Neuron, Volume *77*

Supplemental Information

Distinct Roles of TRP Channels in Auditory

Transduction and Amplification in *Drosophila*

Brendan P. Lehnert, Allison E. Baker, Quentin Gaudry, Ann-Shyn Chiang, and Rachel I. Wilson

Inventory of Supplemental Information

Supplemental Item	Related Figure	Explanation
Figure S1	Figure 3	describes measurements of antennal rotations
Figure S2	Figure 7	explains why type AB JONs may be stretched by both medial and lateral rotations of the antenna
Figure S3	Figure 8	describes evidence that resting transduction is elevated in the *nompC*^{3} mutant
Figure S4	Figure 9	shows that a small and slow component of the generator current is absent in *nompC* mutants
Supplemental Experimental Procedures	n/a	n/a

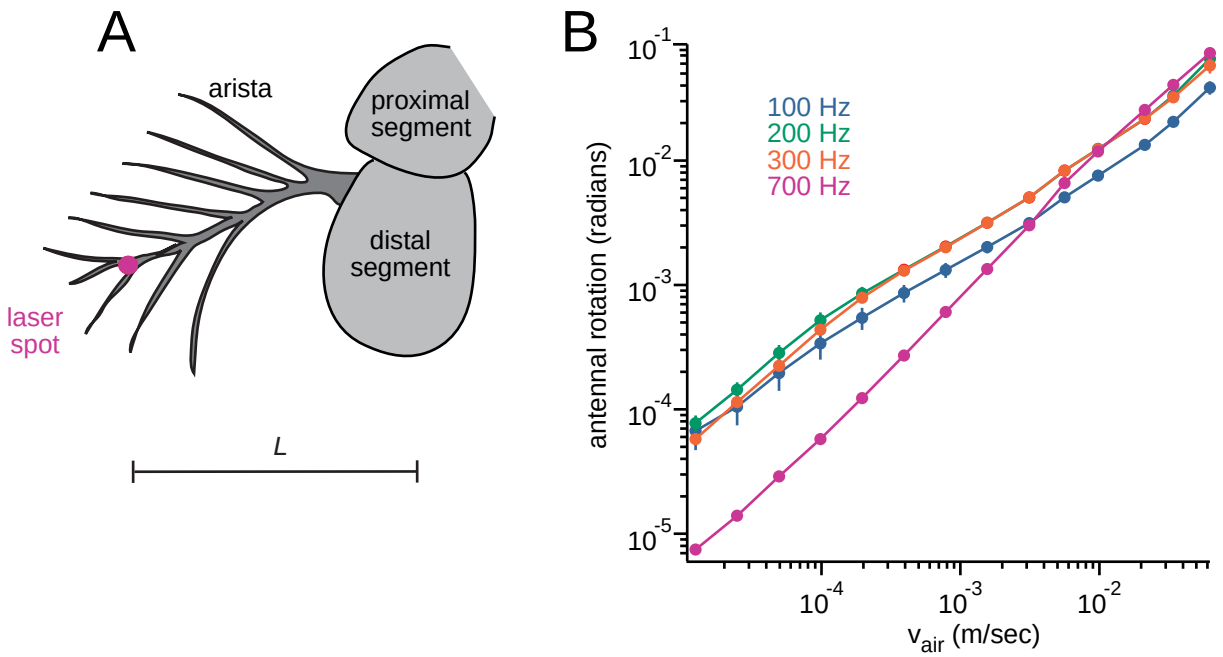

Figure S1. Rotation of the antenna.
(A) The distal portion of the antenna rotates in response to a sound stimulus (Gopfert and Robert, 2001). To measure antennal rotation, we used a laser Doppler vibrometer to record displacement ($D(t)$) during sound stimulation, placing the laser spot at the most distal branchpoint of the arista. We also measured the length of the aristal lever arm (L) from the laser spot to the rotational center of the distal antennal segment. We then used the small angle approximation ($\omega(t)=D(t)/L$) to calculate the rotation of the antenna (see also Supplemental Experimental Procedures).
(B) The amplitude of antennal rotation in response to pure tone stimuli at a range of sound particle velocities and sound frequencies. These measurements are consistent with previously published values (Gopfert et al., 2006).

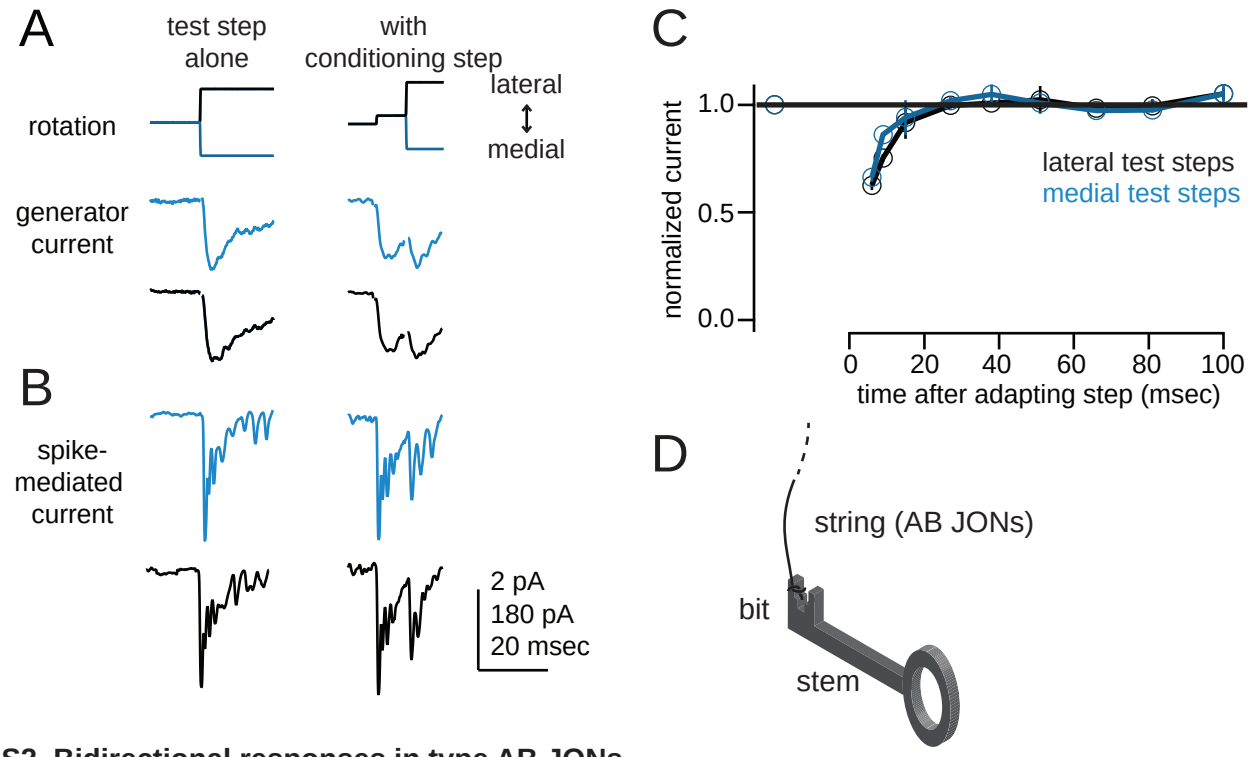

Figure S2. Bidirectional responses in type AB JONs.
(A) A large piezoelectric test step (0.032 radians) in either the medial or lateral direction evokes a saturating level of generator current in the GFN. Test steps are applied either alone, or else after a conditioning step in the lateral direction (0.008 radians). Brief stimulus artifacts in the generator currents have been blanked for clarity. The test step evokes the same maximum current, with or without the conditioning step.
(B) Spike-mediated current recorded in the GFN in response to the same stimuli (i.e., in the absence of TTX). Note that the adapting step suppresses the response to the test step, which no longer reaches the maximum level. This suppression likely reflects spike adaptation in JONs, because it does not occur in the generator currents. Note that the extent of adaptation is the same regardless of whether the test step is in the same or opposite direction as the adapting step.
(C) Group data showing spike-mediated current, normalized to the average test step response in each recording (n=3). Note that there is clear cross-adaptation between medial and lateral steps. Because spike adaptation is a cell-autonomous process, this result suggests that individual type AB JONs are depolarized by both medial and lateral steps.
(D) Schematic representation of the arrangement of these JONs in Johnston's organ. Sound causes the distal segment of the antenna to rotate on its long axis, like a key rotating about its stem in a lock (Gopfert and Robert, 2001). The bit of the key is inserted into Johnston's organ, where it attaches via connective structures to JON dendrites. An individual JON is like an elastic string which is tied to the bit at one end, with the opposite end anchored. Some JONs are positioned as shown, lying in the plane of the bit's rotation, and oriented so that they are stretched by rotations in either direction (Kamikouchi et al., 2006). This description appears to apply to at least some type A JONs, and possibly also some type B JONs.

Bidirectional activation of type A/B JONs was predicted on the basis of their anatomy (Kamikouchi et al., 2006), and these results provide functional evidence in favor of this prediction. It should be noted that not all JONs are bidirectional. Calcium imaging of the JON array reveals opponent populations that are either excited by medial rotations and inhibited by lateral rotations, or vice versa (Kamikouchi et al., 2009). These "opponent populations" of JONs appear to belong to the CE subgroup (Yoruzu et al., 2009).

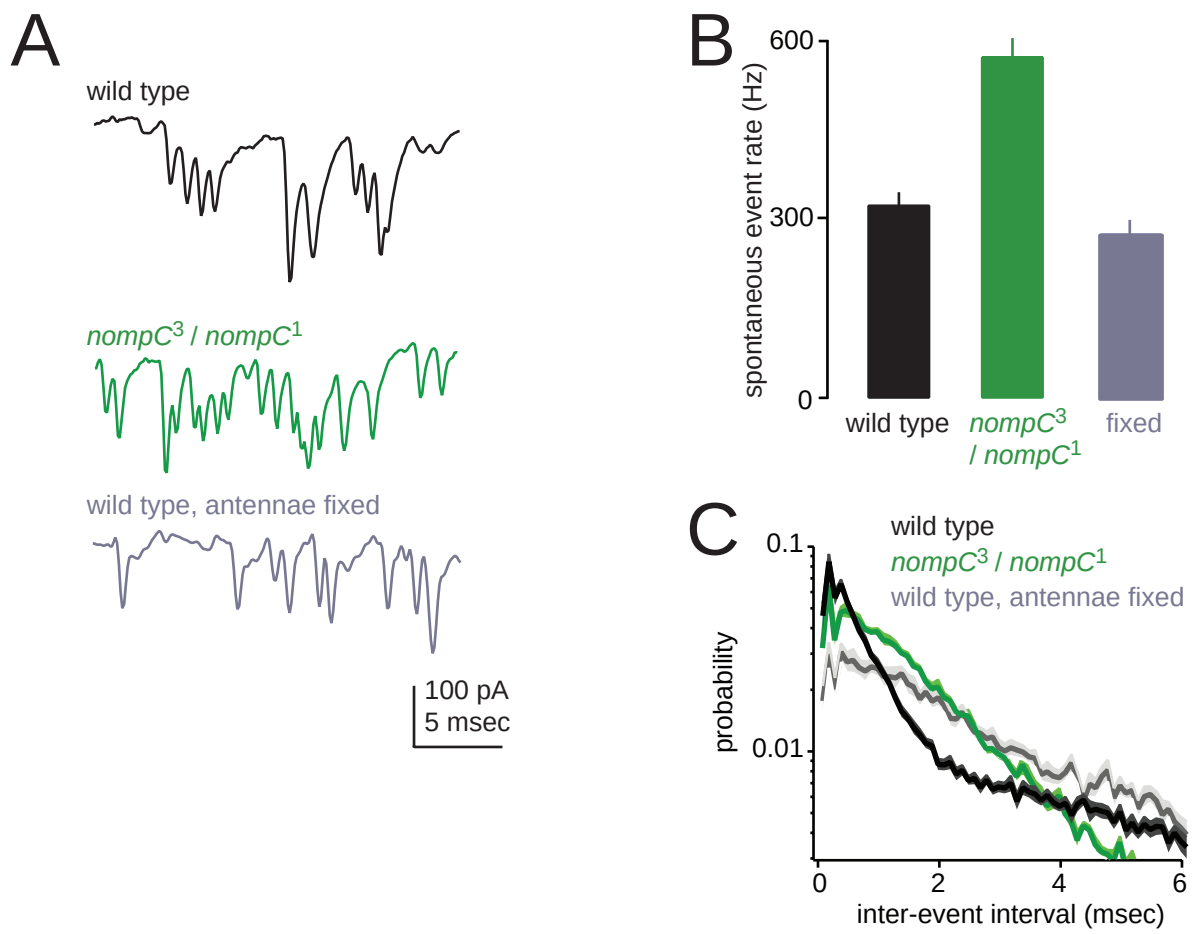

Figure S3. Spontaneous event rate is increased in *nompC* mutants.
(A) Representative recordings of spontaneous events (i.e., putative JON spikes, recorded from the GFN with TTX omitted from the bath). The amplitude of isolated single events is similar in three different experimental conditions: wild type, *nompC* mutant, and wild type with the distal segment of the antennae fixed in place with drops of glue. This is consistent with the idea that events represent JON spikes. Wild type recordings also show occasional large deflections, suggesting the simultaneous arrival of several coincident events.
(B) Group data showing spontaneous event rate averaged across recordings, ± SEM. Event rate is significantly higher in the *nompC* mutant as compared to wild type, but not significantly different when the antennae are fixed as compared to when the antennae are free ($p<0.01$ and $p>0.05$ respectively, *t*-tests, $n=15$ wild type, 9 *nompC* mutant, 7 antennae fixed). There is evidence that some transduction channels are open at rest, even in the absence of sound (see Discussion; also Albert et al., 2007; Kamikouchi et al., 2009). Thus, the elevated rate of spontaneous events in the *nompC* mutant suggests that resting transduction is abnormally high.
(C) Histograms showing mean inter-event interval distributions averaged across recordings, ± SEM (semilog scale). This plot shows the probability of a given inter-event interval for each condition; shown this way, events generated by a random (Poisson) process will appear linear. This is the case for the *nompC* mutant and antenna-fixed distributions, suggesting that spontaneous events are driven by stochastic openings of transduction channels. By contrast, the wild type distribution shows a predominance of shorter inter-event intervals, implying that these events are non-random, and likely to be triggered by small antennal movements.

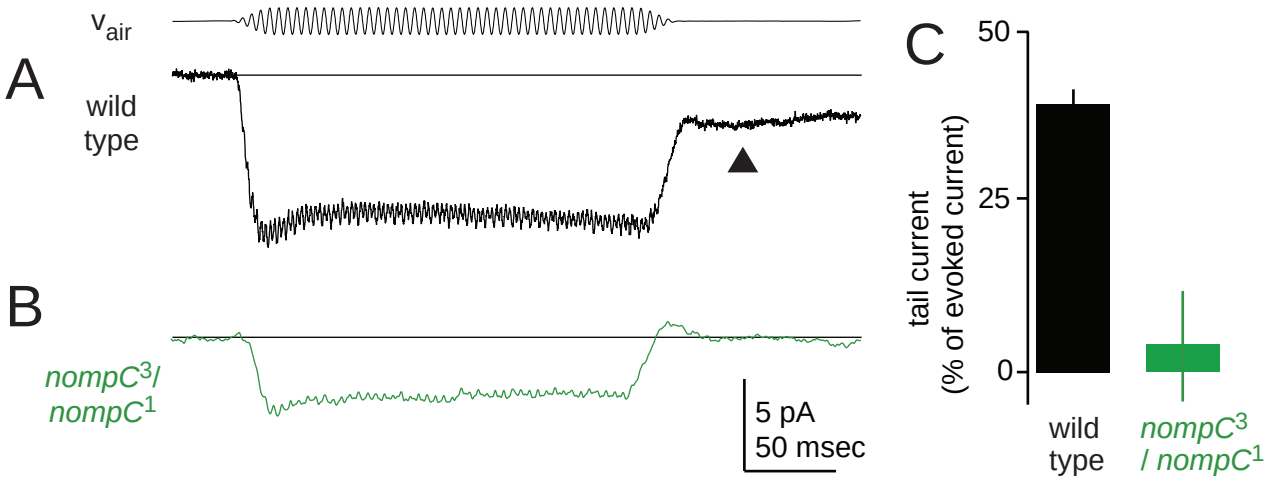

Figure S4: Loss of NompC eliminates a small and slow component of the generator current.
(A) Sound-evoked generator current from a representative wild type preparation. The sound stimulus is a 200 Hz tone (intensity 0.0059 m/sec). There is a persistent current after sound offset that decayed back to baseline with a time constant of 1 - 3 sec. We term this the "tail current". The arrowhead marks the time point at which the current amplitude was measured in panel C.
(B) Same as (A), but for a *nompC*^{3} / *nompC*^{1} preparation. Note that the tail current is absent.
(C) Group data averaged across many experiments like those in (A-B) (n=9 wild type, 9 *nompC*^{3} / *nompC*^{1}) The average amplitude of the tail current is significantly different in *nompC*^{3} / *nompC*^{1} mutants as compared to wild type ($p<0.005$, t-test). Tail current was calculated as the mean current over a 10-msec window starting 30 msec after sound offset, and was expressed as percentage of the mean sound-evoked current over the entire unramped portion of the preceding tone.

These results show that the tail current following a sound stimulus requires NompC. One possibility is that the tail current represents current through this channel. Alternatively, the tail current may represent current through the transduction channel. In this latter scenario, the tail current is missing in the absence of NompC because NompC is involved in changing the forces acting on the transduction channel over the course of the sound response, such that the level of resting current is increased after sound offset, yielding a "tail". Importantly, the tail current disappears in the *nanchung* or *inactive* mutants (see Figure 4).

SUPPLEMENTAL EXPERIMENTAL PROCEDURES

Fly stocks and genetic manipulations

Flies were reared on cornmeal agar media at 25°C. Males were used for recordings from *shakB*^{2} mutants and in the *inactive* rescue experiments, whereas in all other cases the experimental animals were female. Fly stocks were previously described as follows: "Dickinson wild-caught" stock (Frye and Dickinson, 2004),*UAS-iav* (Kwon et al., 2010), *UAS-dicer2* and *UAS-DmNa$_v$-RNAi* (Dietzl et al., 2007; Nagel and Wilson, 2011), *JO-AB-Gal4* (also known as *JO15*) and *JO-CE Gal4* (also known as *JO31*; Kamikouchi et al., 2006), *UAS-nompC-L:GFP* (Cheng et al., 2010), *shakB*^{2} (Baird et al., 1990), *nan-Gal4* and *nan*^{36a} (Kim et al., 2003), *nompC*^{3} and *nompC*^{1} (Walker et al., 2000), *iav*^{1} (Gong et al., 2004), *UAS-CD8:GFP* (Lee and Luo, 1999). The *nan*^{36a} and *UAS-CD8:GFP* stocks were obtained from the Bloomington Drosophila Stock Center at Indiana University, and *UAS-DmNa$_v$-RNAi* was obtained from the Vienna Drosophila Resource Center (stock 6131). Due to their impaired ability to eclose from the pupal case, *nompC*^{3}/*nompC*^{1} flies were transferred to damp filter paper as third instar larvae and allowed to pupate. We used transheterozygotes of two null alleles (*nompC*^{3}/*nompC*^{1}) because these flies were marginally more viable than homozygous nulls. Also, this helps ensure that any phenotype reflects the loss of NompC rather than a background mutation.

We used GAL4 lines that selectively labeled the GFN to target these cells for patch clamp recordings in most experiments. Line *G0066-Gal4* drives expression specifically in the GFN. Line *G0117-Gal4* drives strong expression in the GFN, together with weaker expression in several Giant Commissiural Interneurons (GCIs). The GFN is easily discriminable from the GCIs when the brain is viewed from the posterior side using a 40× water immersion objective, and so the presence of GFP expression in the GCIs did not interfere with our ability to target our electrodes to the GFN. In experiments where the voltage-gated sodium channel alpha subunit (*DmNa$_v$*) was knocked down in JONs using transgenic RNAi, the knockdown transgene was also expressed in the GFN (and in other neurons of the giant fiber system that express Gal4 under the control of the *G0117-Gal4* line). This was unavoidable due to the need to label the GFN with GFP in the same flies. To determine whether expression of the knockdown transgene in the GFN had any effect, we performed experiments where the JON Gal4 driver was omitted but the GFN Gal4 driver was present. These control experiments showed that there was no effect of *DmNa$_v$* knockdown in the GFN alone, demonstrating that the phenotypes observed in Figure 2D,E and Figure 3B,C were due to knockdown in the JONs, not the GFN. Thus, for clarity, we refer in the text to the *DmNa$_v$* knockdown genotype as "selective JON knockdown."

Microphone calibration

As a sound wave propagates, it produces changes in the pressure and velocity of particles in the medium. The *Drosophila* auditory system is sensitive to the particle velocity component of the sound wave (Robert and Hoy, 2007). For this reason, we need to calibrate a microphone that is sensitive to particle velocity. To do this, we calibrated a particle velocity microphone against a pressure sensitive microphone of known sensitivity under conditions where these two quantities are related to each other through the acoustic impedance of the medium (i.e., in the acoustic far field; Cator et al., 2009). We presented 1-sec pure tones at 7 frequencies and 4 intensities using a function generator driving an amplifier (Crown XLS202) and speaker (Morel SCM634). We simultaneously acquired the voltage responses of two microphones. First, we used a pressure microphone (Brüel & Kjaer 4176, used with preamplifier type 2671-W-001). This microphone and preamplifier have a flat frequency response (+/- 0.1 dB) with phase delays of 3 - 10° relative to the sound field in the range of calibration. The voltage output of this microphone (V_{BK}) is related to the sound pressure ($p(t)$) by a sensitivity factor k_{BK} which is independent of frequency (equal to 49.4 mV/Pa, according to the manufacturer's specifications):

$$p(t) = V_{BK}(t)/k_{BK}$$

We used a second microphone (Knowles Electronics NR-23158) whose voltage output is related to the pressure gradient in space ($\partial p/\partial x$) by a sensitivity factor (k_{KE}) that depends on frequency. The sensitivity factor of this

microphone is what we want to measure. Measuring the pressure gradient allows us to compute the particle velocity (see below), which is the relevant feature of a sound stimulus for the *Drosophila* antenna.

The calibration was performed outside in a large grassy open space to minimize sound reflection. The two microphones were placed 4 meters away from the speaker, with the front face of the Knowles Electronics microphone perpendicular to the direction of sound propagation.

Under far field conditions, the time-varying particle velocity component ($u(t)$) of a sound wave is in phase with the pressure component $p(t)$ and is related to it through the density of air ρ (1.21 kg/m^3) and the speed of sound c (340 m/s):

$$p(t) = u(t)\rho c$$

Thus

$$\frac{\partial p}{\partial t} = \frac{\partial u}{\partial t}\rho c$$

The pressure gradient in space is related to gradient in time by the speed of sound:

$$\frac{\partial p}{\partial x} = \frac{\partial p}{\partial t} \cdot \frac{1}{c}$$

And so

$$\frac{\partial p}{\partial x} = \frac{\partial u}{\partial t}\rho$$

Integrating, we obtain

$$\int_0^t \frac{\partial p}{\partial \mathrm{x}}(t)dt = u(t)\rho$$

Recall that the voltage output of the Knowles Electronics microphone (V_{KE}) is proportional to $\partial p/\partial$x. We define a sensitivity factor (k_{KE}) which relates the time integral of V_{KE} to the particle velocity:

$$\int_0^t V_{KE}(t)dt = k_{KE}u(t) = k_{KE} \cdot \frac{p(t)}{\rho c} = k_{KE} \cdot \frac{V_{BK}(t)}{k_{BK}\rho c}$$

Integration of the signal V_{KE} was performed in software. For each test frequency, we measured the Fourier amplitude of the time integral of V_{KE} at that frequency, and also the Fourier amplitude of V_{BK}. Dividing the latter by $k_{BK}\rho c$ and fitting a line gives us the slope k_{KE}:

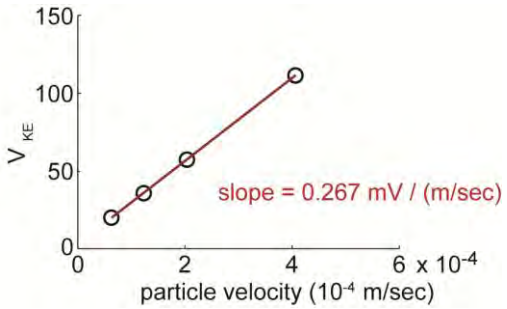

The calibrated sensitivities of the microphone for all frequencies in our test set are shown below (top panel):

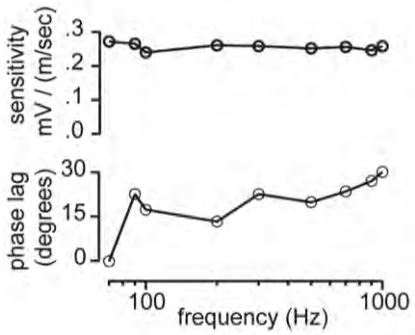

This plot also shows the phase delays between the integrated signal V_{KE} and V_{BK} (bottom panel). To determine the phase of the particle velocity wave, we took account of these phase delays, plus the phase delay of the Brüel & Kjaer microphone and preamplifier (according to manufacturer's specifications). The net phase delays of the microphone and signal conditioning system were measured and corrected for in the traces displayed in all figures (12° for 100 Hz, 18° for 200 Hz, 28° for 300 Hz, 37° for 700 Hz).

During this calibration procedure, the output of both microphones was amplified and filtered (Stanford Research SR560, 6dB/octave bandpass with 1 Hz and 30kHz cutoffs) prior to digitization (Measurement Computing USB-1208FS). The relative time delay between digitization of the two channels was measured and subtracted from the second channel.

In order to generate several sets of tones where all the tones in a set have approximately the same particle velocity amplitude at the fly, we generated sound files where the amplitude of the voltage output for each tone was adjusted to achieve this. This adjustment is necessary because the output of the speaker is not necessarily flat with frequency, and because the particle velocity of high-frequency tones decays more rapidly with distance than the particle velocity of low-frequency tones. The plot below shows that particle velocity amplitudes for each frequency within a set were approximately equal, as measured with the Knowles Electronics (velocity) microphone at the position of the fly:

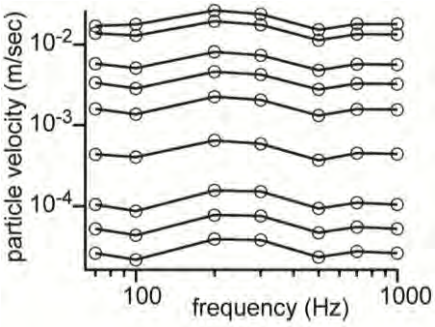

Because the speaker was positioned differently for presentation to the right and left antenna, we created different sound files with slightly different amplitude adjustments for these two speaker positions. As expected, when we instead place the Brüel & Kjaer (pressure) microphone at the fly's position, we see a discrepancy between the output of the two microphones which depends on frequency:

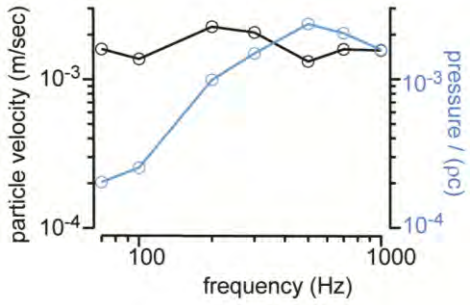

This reflects the fact that the near field is defined in terms of the wavelength of the sound, and the extent of the near field is smaller for high-frequency sounds. All particle velocity levels described in this study are expressed as the mean-to-peak amplitude of the measured particle velocity waveform.

Sound isolation and delivery

All electrophysiological, behavioral, and laser Doppler vibrometry recordings were made in a custom-built sound isolation chamber lined with 2" of medium density fiberboard interleaved with a total of 5.25" urethane composite noise barrier (Sonex). Sound absorbing panels (Realtraps, New Milford, CT) were used to reduce ambient noise in the recording room, and the ventilation system was disabled to reduce low frequency noise. The chamber had an unweighted background noise level of 23 dB SPL (unweighted measurement restricted to 0.05-2 kHz), which is well below the *Drosophila* behavioral and electrophysiological far-field sound threshold

(Figure 1). Pure tones were synthesized in Matlab (Mathworks). Sounds were delivered through a Crown D-45 amplifier driving a 89.5 mm diameter speaker (Scan-Speak Discovery 10F/4424G). The speaker was mounted in a grounded copper mesh cage to reduce electrical noise. The speaker was positioned ~230 mm from the fly and could be easily transferred between one of two fixed mount points, which corresponded to locations roughly orthogonal to the left and right arista. In electrophysiological experiments, the speaker was always positioned orthogonal to the arista which was ipsilateral to the recorded GFN, or to the recorded antennal nerve. In behavioral experiments, the speaker was always positioned orthogonal to the fly's right arista.

Behavioral experiments

The data in Figure 1B-D were collected using a fly stock recently derived from wild-caught *Drosophila melanogaster* ("Dickinson wild-caught stock"), because these flies showed more robust running than inbred stocks. For all behavioral experiments, virgin females were collected from sparse cultures 1-2 days prior to testing and housed in small groups. On the night before the experiment, the head was immobilized by gluing it to the thorax with UV-curable adhesive (KOA 300, Kemxert, York PA). On the day of the experiment, flies were briefly anesthetized on a cold steel block and attached to an insect pin with UV-curable adhesive. The tethered fly was transferred to a dark, sound-insulated test chamber containing a spherical treadmill, which consisted of a ball floating on a cushion of air (diameter = 1/4", 75 mg, HDPE hollow, The Precision Ball Co LTD, UK and Craigs Technology). The fly's tether was attached to a micromanipulator and lowered on to the ball with the aid of cameras positioned on the top, front, and side of the ball. An optical mouse sensor positioned below the ball reported the *x* and *y* position of the ball at 500 Hz. This signal was acquired in Matlab at 3.5 kHz, and subsequently filtered (zero-phase low-pass Butterworth with 100 Hz cutoff) and interpolated at 1 kHz. Traces in Figure 1B are the numerical derivative of the position versus time recordings along the treadmill's forward axis. Sound stimuli consisted of pure tones 250 msec in duration, presented using a speaker placed 21 cm in front and 14 cm to the left of the fly. Each fly was tested in either 240 or 300 trials. These trials were presented in blocks of either 50 or 60 trials. Trials were excluded if the fly did not run for the entire trial. If 20 or more trials were excluded from a given block, the entire block was excluded from analysis. An entire experiment was excluded if more than 3 blocks of trials were excluded. The mean change in forward running velocity was defined as the trial-averaged velocity during a 15 msec period beginning 50 msec after sound onset, minus the trial-averaged velocity during a 15 msec period immediately before sound onset.

Antennal nerve field potential recordings

The fly was immobilized with wax and UV-curable adhesive in the end of a trimmed 200-μL micropipette tip. The lateral face of the second antennal segment was glued to the head to stabilize the electrode insertion site. A saline-filled quartz recording electrode (30 - 50 MOhm resistance) was inserted in the joint between the first and second antennal segment from the dorsomedial side. A pulled borosilicate glass capillary filled with saline was inserted into the eye to serve as a reference electrode. Field potentials were recorded using an Axopatch 200B amplifier (Axon Instruments) in I=0 mode, low-pass filtered at 2 kHz using the amplifier's internal four-pole Bessel filter, digitized at 10 kHz by a 16 bit A/D converter (National Instruments, BNC-2090A), and acquired in IgorPro (Wavemetrics). Measurements were performed on flies 12 – 48 hours post-eclosion. One recording (out of six) was excluded from analysis because it was insensitive to stimuli that were effective in other recordings.

Laser Doppler vibrometry

Sound-driven antennal movements were measured using a laser Doppler vibrometer (Polytec OFV-5000 equipped with OFV-500, VD-06, and DD-500 decoder boards). A calibrated particle velocity microphone was placed within 3 mm of the fly, such that the stimulus and mechanical response were simultaneously recorded and acquired in IgorPro. We removed the fly's legs and waxed the abdomen to a trimmed 200-μL micropipette tip. UV-curable adhesive was used to fix the head to the body, and also to fix the second antennal segments to the head. The micropipette tip was mounted on a micromanipulator, and was visualized using a CCD video imaging system coupled to a 20× objective (Polytec OFV-534, Mitutoyo MP20×). Prior to sound stimulation,

the fly was translated using the micromanipulator until the laser measurement spot coincided with the most distal branch point of the arista. Flies were excluded from analysis of sound-induced antennal rotations if the free fluctuations of the antenna showed the higher-frequency mechanical resonance and reduction in amplitude characteristic of dead flies. The rotations produced by piezoelectric actuation of the antenna were calculated from measurements of the motion of the stimulus probe. The traces in Figure 6 and 8 show the motion of the piezoelectric stack, measured at the actuated end surface with the probe attached. The traces in Figure 7 and 9 show the commanded motion of the stack, not measured motion, because in some experiments the laser Doppler vibrometer reported an artifactual drift which was not observed in the camera image and which exceeded the specified range of the piezoelectric device.

Whole-cell recordings

Recordings were made 6-18 hours post-eclosion because older flies showed substantially smaller sound-evoked currents than flies <18 hours old. Currents were recorded from the Giant Fiber Neuron (GFN) *in vivo* using the whole-cell patch-clamp technique in voltage-clamp mode. Stable auditory responses from the GFN could be recorded for 1-4 hours. Flies were briefly cold anesthetized and immobilized using UV-curable adhesive in a hole cut into a piece of titanium foil within a larger flat recording platform. The upper side of the fly's head (above the platform) was bathed in oxygenated saline, while the underside of the head and both antennae (together with most of the thorax and all of the abdomen) remained dry. The posterior cuticle of the head was surgically removed to expose the posterior side of the brain, and the perineural sheath was removed with fine forceps. The preparation was then placed under an upright compound microscope equipped with an Hg arc lamp and a 40× water immersion objective (Olympus BX51). Prior to beginning a recording, the platform was oriented in a standard configuration with respect to the sound stimulus by rotating it until the fluorescently labeled GFN cell bodies were level in the field of view. After a stable whole-cell recording was obtained from the GFN under visual control, the microscope condenser was removed prior to sound stimulation to better mimic the sound field in the *in situ* particle velocity calibration.

The external saline solution was composed as previously described (Wilson and Laurent, 2005). The saline was recirculated continuously and was bubbled throughout the experiment with 95% O_2 / 5% CO_2. The internal pipette solution contained (in mM): 111 K-aspartate, 8 HEPES, 0.08 EGTA, 8 BAPTA, 3.2 MgATP, 0.4 Na_3GTP, 1.6 KCl, 10 biocytin hydrazide. The pH of the internal solution was adjusted to 7.3 with KOH and the osmolarity was adjusted to 265 mOsm. In the majority of experiments, the patch pipette was targeted to the GFN based on GFP visualization. In cases where labeling the GFN with GFP was difficult or undesirable, unlabeled GFNs were targeted based on their large nucleoli and cell body position, and biocytin fills were imaged *post hoc* to confirm that the recorded neuron was indeed the GFN.

Voltage-clamped currents were recorded from the GFN with an Axopatch 200B amplifier. Cells were clamped at -60 mV. The typical input resistance of the GFN was 50-100 MOhm, and estimates of access resistance based on the height of the fast current transient during test voltage steps were 8-20 MOhm. We saw no evidence of sodium spikes in any of our GFN recordings, and no evidence of active conductances when holding the cell around its resting potential in voltage-clamp mode. Pilot experiments comparing wild type flies and the nan^{36a} mutants showed little difference in the power spectra at frequencies above ~1.5 kHz, so all subsequent experiments were performed with the amplifier's internal four-pole Bessel filter set to a 2 kHz cutoff frequency. Data were digitized at 10 kHz by a 16 bit A/D converter (National Instruments, BNC-2090A) and acquired in Igor Pro (Wavemetrics).

Three observations suggest that we have some degree of control over the voltage in the GFN dendrite in our recordings. First, recorded unitary events decay ~2.3 times more rapidly in voltage clamp mode than in current clamp mode (data not shown). Second, sound stimuli cause the GFN to spike in current clamp mode, but not in voltage clamp mode, provided that the membrane is not depolarized above -30 mV (data not shown; see also Tootoonian et al., 2012). Third, the frequency and amplitude of events recorded in the GFN was similar for holding potentials between -90 mV and -40 mV.

Immunohistochemistry

To visualize NompC:GFP localization within JONs (Figure 4E), antennae were dissected away from the head and fixed for 12 minutes in 4% aqueous paraformaldehyde at room temperature. After washing in PBS and incubation in blocking solution (5% goat serum in PBST), samples were incubated in a primary antibody solution for 24 hours containing 1:300 chicken anti-GFP (Invitrogen) and 1:300 mouse 21A6 antibody (which labels the ciliary dilation, Lee et al., 2010; Developmental Studies Hybridoma Bank), followed by a 2-day incubation in secondary antibody solution containing 1:1000 anti-chicken:AlexaFluor488 and 1:1000 anti-mouse:AlexaFluor633 (Invitrogen). Antennae were then mounted in Vectashield (Vector Laboratories) and visualized on a Zeiss LSM 510 laser scanning confocal microscope. All other whole-mount immunofluorescence microscopy (in Figure 5, and in experiments to verify the identity of the GFN when it was not labeled with GFP) was performed as previously described (Wilson and Laurent, 2005).

Piezoelectric antennal movement

Whole-cell recordings were performed as described in the previous sections, except that in these preparations the second antennal segment on the right side of the fly's head was glued to the titanium foil, leaving only the third antennal segment free to rotate. A piezoelectric stack was fixed on a hollow titanium arm (McMaster-Carr) and mounted on a micromanipulator (MP-225, Sutter Instruments). Elastic lashing between the manipulator arm and microscope stage was used to shift the intrinsic 70 Hz mechanical resonance of the mounted assembly to 400-600 Hz and reduce the magnitude of the arm's resonant motion. Movement of the piezoelectric stack was transferred to the fly's antenna using a tungsten stimulus probe (#UEWLGGSE5N1J, Frederick Haer & Co). The tip of the probe was visualized using a custom-built imaging system (consisting of a miniature video camera and a 50× air objective) that was mounted in place of the condenser in the BX-51 microscope (i.e., under the titanium foil) after the whole-cell recording was obtained. To achieve a high contrast image of the arista and probe tip, the preparation was back-lit using the upright compound microscope's epifluorescence system. The probe tip was slowly maneuvered from a position below the fly into contact with the arista. In some experiments, we used a quick-drying two-component epoxy to attach the probe to the arista. In most experiments, however, we instead relied on the tendency for the probe to spontaneously adhere to the arista. In all cases, high-magnification videography was used to observe the motion of the arista and attached probe (in response to a train of 14.2-μm lateral and medial steps, the largest step in our set) for 2 -3 minutes prior to attempting GFN recording and after the termination of the recording. Preparations where the probe was observed to break contact with the arista were discarded; thus, this stimulus represents a displacement clamp of the arista. The probe tip was targeted to the distal-most branch point of the arista, the same location targeted in the laser Doppler vibrometry measurements. Aristal displacements were converted into rotations using the small angle approximation, where the length of the rotating lever arm was taken as the average measured length from the most distal branchpoint of the arista to the midline of the third antennal segment (150 μm; see Figure S1). We report rotation in the main text (rather than displacement) because this measure should not depend on the position of the probe tip on the arista. The series of rotation steps we used corresponds to the following series of displacments of the probe tip (in nm): 74, 148, 296, 593, 1180, 2370, 4740, 10430, 14200. Step rotations were presented every 0.8 sec in a deterministic, pseudorandom order by instantiating a random number generator with a seed value that was the same for every experiment. Experiments were included in the data set if they contained at least 800 trials.

Piezoelectric commands were synthesized in software, delivered as an analog output at 10 kHz, and filtered with an 8-pole bessel filter (Frequency Devices LPF 900). A filter cutoff frequency of 3 kHz was chosen to stay within the specified operating limits of the high-current piezo amplifier (Physik Instrumente E-501, E-505). The amplifier drove a housed piezoelectric stack (P-810.30, 1 μF capacitance, 12 kHz unloaded resonance frequency, Physik Instrumente). Laser Doppler vibrometric measurements of the displacement of the piezoelectric stack showed a linear relationship to the applied voltage command with a scale factor of 474 nm/V. Hysteresis was less than 10% of the commanded movement for the protocols employed in this study. For all step stimuli, the rise time (from 10% of maximum to 90% of maximum) as measured with the laser

Doppler vibrometer was 300 – 400 microseconds. Piezoelectric steps caused a transient artifact in the electrophysiological recordings, and this is blanked for clarity in the traces displayed in the figures.

Data analysis

Unless otherwise noted, all analyses were performed in IgorPro. Spontaneous events (i.e., putative JON spikes) were detected with a shape template using an automated routine. The initial event template consisted of a single event, and was selected from a portion of the trace that was not included in the analysis. This template was used to detect well-isolated events in the entire recording, which were then averaged together to yield a new template, and this was subsequently used to perform the final analysis. Recordings were excluded from the spontaneous event analysis if the amplitude of the unitary event was less than 65 pA, as it was difficult to accurately identify events in these cases. All generator currents displayed in the figures represent averages across many trials with the same stimulus in the same cell, and measurements of generator currents were always performed on trial-averaged data. Trial-averaged generator currents were smoothed by convolving them with a 0.5-msec Gaussian prior to analysis or display in figures. The peak current evoked by a step stimulus was taken as the minimum or maximum in the 7 msec after step onset. The rise time of generator currents was calculated as the time elapsed between 10% of maximum and 90% of maximum. The Fast Fourier Transform (FFT) was used to calculate the antenna's displacement during a sound stimulus, the magnitude of the particle velocity sound stimulus, and the 1f and 2f signal in the frequency domain representation of generator currents.

Mean values with error bars in all figures represent averages across cells, and all error bars represent the SEM computed across cells. Statistical analysis was performed using either Matlab or R version 2.9.2 with the companion to applied regression package (obtained from http://www.r-project.org/). Fisher's F-test (with a $p>0.05$ criterion) was used to test for homoskedasticity prior to performing any t-tests. If the two sample distributions were not homoskedastic, we performed Welch's two-sample t-test.

Simulations

The relationship between transduction and rotation was modeled as a pair of hyperbolic functions, where the two functions correspond to the two directions of motion that can gate transduction. Each pair of curves specifies the amount of current for a given rotation:

$$c(t) = \frac{r(t)}{r(t)+\sigma} \quad \text{for } r>0$$

$$c(t) = \frac{-r(t)}{-r(t)+\sigma} \quad \text{for } r<0$$

where $r(t)$ is rotation, $c(t)$ is current, and σ is a semi-saturation constant (i.e., the level of rotation that produces half-maximal current). The values of σ are 30 for the wild type simulation and 100 for the *nompC* mutant simulation (arbitrary rotation units). This means that all the curves saturate at the same level, but larger rotations are required to saturate the *nompC* mutant responses. The transduction-rotation curves are shifted 16 units to the left for the *nompC* mutant. The peak-to-mean amplitude of the simulated rotation stimulus is 50 units. The x-axes of the simulated curves shown in Figure 8E-F range from -800 to +800 units. There are 33 time steps per stimulus cycle in the simulation. In our GFN recordings, the JONs are not voltage-clamped, meaning that the time course of the voltage deflection in JONs (and thus the signal we record in the GFN) must be a low-pass filtered version of the summed transduction currents. To account for this, we smoothed all the simulated currents by convolving them with a Gaussian function having a standard deviation of 6 time steps. This low-pass filtering is critical to allow the simulation to reproduce the dynamics in the data. The reason why the 2f power diminishes in the *nompC* mutant simulation is that, when the curves are shifted to the left, leftward rotations traverse the steep area of the curves near their intersection point, creating rapid fluctuations in current that are strongly attenuated by the low-pass filtering.

Note that the minimum point in the curves does not necessarily correspond to zero transduction. Indeed, there is evidence that some transduction channels are open at rest (Albert et al., 2007; Kamikouchi et al., 2009).

Thus, the "min" current level may be taken as corresponding to an open probability of the transduction channel greater than zero.

The goal of this model was only to recapitulate certain qualitative aspects of the biological data. We did not aim to recapitulate the data quantitatively, and so we did not assess the goodness of fit. All simulations were performed in IgorPro.

REFERENCES FOR SUPPLEMENTAL EXPERIMENTAL PROCEDURES

Albert, J.T., Nadrowski, B., and Göpfert, M.C. (2007). Mechanical signatures of transducer gating in the Drosophila ear. Curr Biol *17*, 1000-1006.

Baird, D.H., Schalet, A.P., and Wyman, R.J. (1990). The Passover locus in Drosophila melanogaster: complex complementation and different effects on the giant fiber neural pathway. Genetics *126*, 1045-1059.

Cator, L.J., Arthur, B.J., Harrington, L.C., and Hoy, R.R. (2009). Harmonic convergence in the love songs of the dengue vector mosquito. Science *323*, 1077-1079.

Cheng, L.E., Song, W., Looger, L.L., Jan, L.Y., and Jan, Y.N. (2010). The role of the TRP channel NompC in Drosophila larval and adult locomotion. Neuron *67*, 373-380.

Dietzl, G., Chen, D., Schnorrer, F., Su, K.C., Barinova, Y., Fellner, M., Gasser, B., Kinsey, K., Oppel, S., Scheiblauer, S.*, et al.* (2007). A genome-wide transgenic RNAi library for conditional gene inactivation in Drosophila. Nature *448*, 151-156.

Frye, M.A., and Dickinson, M.H. (2004). Motor output reflects the linear superposition of visual and olfactory inputs in Drosophila. J Exp Biol *207*, 123-131.

Gong, Z., Son, W., Chung, Y.D., Kim, J., Shin, D.W., McClung, C.A., Lee, Y., Lee, H.W., Chang, D.J., Kaang, B.K.*, et al.* (2004). Two interdependent TRPV channel subunits, inactive and Nanchung, mediate hearing in Drosophila. J Neurosci *24*, 9059-9066.

Kamikouchi, A., Inagaki, H.K., Effertz, T., Hendrich, O., Fiala, A., Göpfert, M.C., and Ito, K. (2009). The neural basis of Drosophila gravity-sensing and hearing. Nature *458*, 165-171.

Kamikouchi, A., Shimada, T., and Ito, K. (2006). Comprehensive classification of the auditory sensory projections in the brain of the fruit fly Drosophila melanogaster. J Comp Neurol *499*, 317-356.

Kim, J., Chung, Y.D., Park, D.Y., Choi, S., Shin, D.W., Soh, H., Lee, H.W., Son, W., Yim, J., Park, C.S.*, et al.* (2003). A TRPV family ion channel required for hearing in Drosophila. Nature *424*, 81-84.

Kwon, Y., Shen, W.L., Shim, H.S., and Montell, C. (2010). Fine thermotactic discrimination between the optimal and slightly cooler temperatures via a TRPV channel in chordotonal neurons. J Neurosci *30*, 10465-10471.

Lee, T., and Luo, L. (1999). Mosaic analysis with a repressible cell marker for studies of gene function in neuronal morphogenesis. Neuron *22*, 451-461.

Nagel, K.I., and Wilson, R.I. (2011). Biophysical mechanisms underlying olfactory receptor neuron dynamics. Nat Neurosci *14*, 208-216.

Robert, D., and Hoy, R.R. (2007). Auditory systems in insects. In Invertebrate Neurobiolology, G. North, and R.J. Greenspan, eds. (Cold Spring Harbor, NY, Cold Spring Harbor Laboratory Press), pp. 155-184.

Tootoonian, S., Coen, P., Kawai, R., and Murthy, M. (2012). Neural representations of courtship song in the Drosophila brain. J Neurosci *32*, 787-798.

Walker, R.G., Willingham, A.T., and Zuker, C.S. (2000). A Drosophila mechanosensory transduction channel. Science *287*, 2229-2234.

Wilson, R.I., and Laurent, G. (2005). Role of GABAergic inhibition in shaping odor-evoked spatiotemporal patterns in the Drosophila antennal lobe. J Neurosci *25*, 9069-9079.